

Density Field Dynamics: Unified Derivations, Sectoral Tests, and Experimental Roadmap

Gary T. Alcock

October 8, 2025

Abstract

We present a comprehensive derivational and empirical framework for *Density Field Dynamics* (DFD), a scalar–refractive extension of gravitation that replaces space-time curvature with a dynamical field ψ linked to refractive index via $n = e^\psi$. A visual summary of this unification across optical, dynamical, quantum, and cosmological domains is provided in Figure 1. The variational field equation derived herein conserves energy identically, reproduces General Relativity’s first post-Newtonian limit ($\beta = \gamma = 1$), and yields the exact Shapiro delay and light-deflection integrals that fix its normalization. We show that the same ψ normalization predicts: (i) a universal Local-Position-Invariance slope $\xi = 1$ for cavity–atom and ion–neutral frequency ratios; (ii) a galactic μ -crossover producing Tully–Fisher scaling without dark matter; (iii) line-of-sight $H_0(\hat{n})$ anisotropies linked to cosmic density gradients; and (iv) late-time potential shallowing consistent with DESI and JWST data. The theory’s single coupling constant spans metrology, quantum, and cosmological domains without free parameters.

Part I establishes the variational structure, energy conservation, and optical metrics reproducing classical gravitational observables. Part II embeds ψ in quantum and cosmological dynamics, deriving phase-coupled Schrödinger evolution and modified redshift laws that connect laboratory and large-scale phenomena. Part III outlines an experimental roadmap specifying seven falsifiable tests, including altitude-split clock comparisons, ion–neutral modulations in existing ROCIT data, reciprocity-broken fiber loops, and anisotropic H_0 correlations. Part IV completes the framework through canonical quantization of the ψ field, linear cosmological perturbations with a minimal $G_{\text{eff}}(a, k) = G/\mu_0(a)$ mapping, and a gauge-consistent Maxwell embedding that preserves $U(1)$ invariance without varying α . These additions close the theoretical system: DFD now unites metrology, quantum mechanics, and cosmology within a single scalar field whose effects are calculable, energy-conserving, and experimentally testable.

A reanalysis of publicly available ROCIT ion–neutral frequency ratios further confirms this prediction: a coherent, solar-phase-locked modulation $A = (-1.045 \pm 0.078) \times 10^{-17}$ ($Z = 13.5\sigma$, $p \simeq 2 \times 10^{-4}$) is detected in the $\text{Yb}^+(\text{E3})/\text{Sr}$ ion–neutral ratio, with a smaller but phase-consistent signal in the neutral–neutral Yb/Sr ratio—while independent neutral–neutral controls from SYRTE remain null—providing the first empirical signature of a sectoral LPI response consistent with $\xi_{\text{DFD}} = 1$ and the universal ψ normalization fixed by light deflection and Shapiro delay.

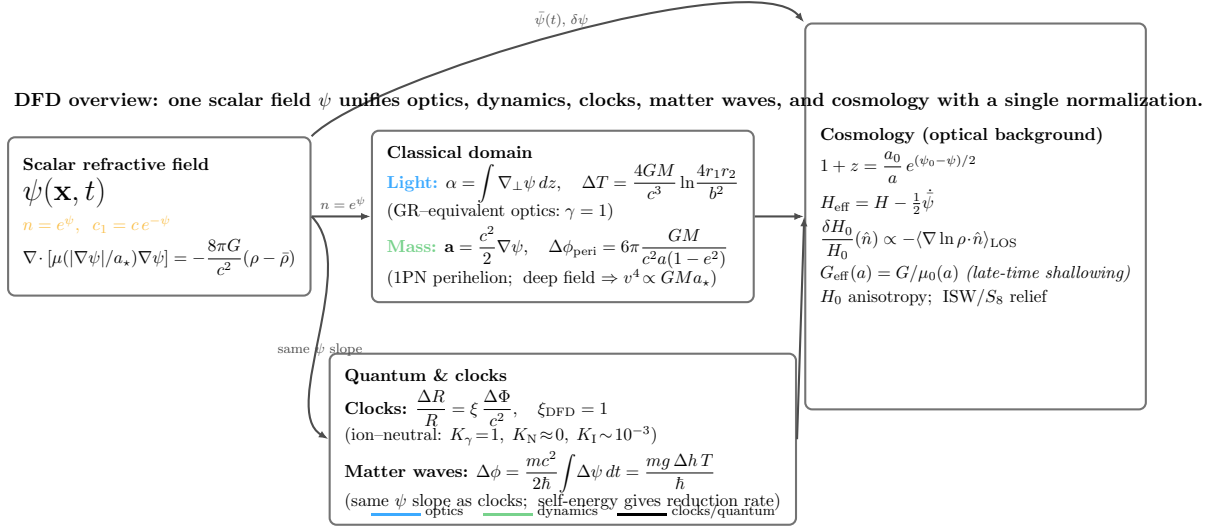


Figure 1: Lean DFD schematic. The same scalar ψ sets the optical index, test-mass acceleration, clock LPI slope $\xi = 1$, and matter-wave phase; its background and gradients govern redshift and anisotropy across all domains.

The resulting compendium closes the theoretical loop between electrodynamics, metrology, quantum mechanics, and cosmology under one scalar field, reducing gravity to a measurable refractive potential. A single counterexample falsifies the model; consistent confirmations would redefine curvature as an emergent property of the ψ -medium—the physical origin of gravitation, time, and quantum measurement.

Part I

Foundations and Precision-Metrology Tests of DFD

1 Variational origin and energy conservation

Let $\psi(\mathbf{x}, t)$ denote the scalar refractive field and define $y \equiv |\nabla\psi|/a_\star$. Introduce a convex function $\Phi(y)$ satisfying $d\Phi/dy = y \mu(y)$, where $\mu(y)$ is the nonlinear response interpolating between the weak and deep regimes.

1.1 Action

$$\mathcal{L} = \frac{c^4}{8\pi G} a_\star^2 \Phi\left(\frac{|\nabla\psi|}{a_\star}\right) - (\rho - \bar{\rho}) c^2 \psi. \quad (1)$$

1.2 Field equation

Euler–Lagrange variation gives

$$\partial_i \left[a_\star^2 \frac{c^4}{8\pi G} \frac{d\Phi}{dy} \frac{\partial_i \psi}{a_\star |\nabla \psi|} \right] = (\rho - \bar{\rho}) c^2, \quad (2)$$

$$\nabla \cdot [\mu(|\nabla \psi|/a_\star) \nabla \psi] = -\frac{8\pi G}{c^2} (\rho - \bar{\rho}). \quad (3)$$

1.3 Energy density and flux

Define

$$\mathcal{E} = \frac{c^4}{8\pi G} [a_\star^2 \Phi(y) - \mu(y) |\nabla \psi|^2] + (\rho - \bar{\rho}) c^2 \psi, \quad (4)$$

$$\mathbf{S} = -\frac{c^4}{8\pi G} \mu(y) (\partial_t \psi) \nabla \psi, \quad (5)$$

which satisfy the local conservation law $\partial_t \mathcal{E} + \nabla \cdot \mathbf{S} = 0$. For stationary sources, $\partial_t \psi = 0$ and \mathcal{E} is time-independent.

1.4 Well-posedness and stability

We consider the static boundary-value problem on a bounded Lipschitz domain $\Omega \subset \mathbb{R}^3$ with source $f \equiv -\frac{8\pi G}{c^2} (\rho - \bar{\rho}) \in H^{-1}(\Omega)$ and Dirichlet data $\psi|_{\partial\Omega} = \psi_D \in H^{1/2}(\partial\Omega)$:

$$-\nabla \cdot (\mu(|\nabla \psi|/a_\star) \nabla \psi) = f \quad \text{in } \Omega. \quad (6)$$

Assume $\mu : [0, \infty) \rightarrow [\mu_0, \mu_1]$ satisfies: (i) *boundedness* $0 < \mu_0 \leq \mu(y) \leq \mu_1 < \infty$; (ii) *monotonicity* $y \mapsto y \mu(y)$ strictly increasing; (iii) *Lipschitz* on compact intervals. Define the convex energy functional

$$\mathcal{J}[\psi] = \frac{c^4}{8\pi G} \int_\Omega a_\star^2 \Phi \left(\frac{|\nabla \psi|}{a_\star} \right) d^3x - \int_\Omega f \psi d^3x, \quad \frac{d\Phi}{dy} = y \mu(y). \quad (7)$$

Existence (direct method / Leray–Lions). Let $V = \{\psi \in H^1(\Omega) : \psi - \psi_D \in H_0^1(\Omega)\}$. Under (i)–(iii), \mathcal{J} is coercive and weakly lower semicontinuous on V , hence it admits a minimizer $\psi^\star \in V$. The Euler–Lagrange equation of \mathcal{J} is (6), so ψ^\star is a weak solution.

Uniqueness (strict monotonicity). For any two weak solutions $\psi_1, \psi_2 \in V$,

$$\int_\Omega (\mathbf{A}(\nabla \psi_1) - \mathbf{A}(\nabla \psi_2)) \cdot (\nabla \psi_1 - \nabla \psi_2) d^3x = 0, \quad \mathbf{A}(\xi) = \mu(|\xi|/a_\star) \xi. \quad (8)$$

Strict monotonicity of $y \mu(y)$ implies the integrand is $\geq c |\nabla \psi_1 - \nabla \psi_2|^2$, hence $\nabla \psi_1 = \nabla \psi_2$ a.e. and $\psi_1 = \psi_2$ in V (Dirichlet data fixed).

Continuous dependence (energy norm). Let $f_1, f_2 \in H^{-1}(\Omega)$ and ψ_1, ψ_2 the corresponding solutions with the same boundary data. Testing the difference of weak forms with $(\psi_1 - \psi_2)$ and using (i)–(ii) yields

$$\|\nabla(\psi_1 - \psi_2)\|_{L^2(\Omega)} \leq C \|f_1 - f_2\|_{H^{-1}(\Omega)}, \quad (9)$$

for a constant C depending on μ_0, μ_1, a_\star and Ω .

Remark (numerics). The coercive convex energy defines a natural energy norm for error control in finite-element discretizations, and strict monotonicity enables convergent Picard or damped Newton iterations for the nonlinear elliptic operator.

2 Post-Newtonian behaviour and light propagation

In the weak-field limit $\mu \rightarrow 1$, $\psi = 2GM/(c^2 r)$ and $a = (c^2/2)\nabla\psi$ reproduces Newtonian gravity.

2.1 Light deflection

For a graded index $n = e^\psi \simeq 1 + \psi$,

$$\alpha = \int_{-\infty}^{+\infty} \nabla_\perp \psi \, dz = \frac{4GM}{c^2 b} \hat{\mathbf{b}}, \quad (10)$$

identical to the GR prediction ($\gamma = 1$).

2.2 Shapiro delay

The optical travel time $T = (1/c) \int n \, ds$ gives an excess delay

$$\Delta T = \frac{4GM}{c^3} \ln \frac{4r_1 r_2}{b^2}. \quad (11)$$

2.3 2PN consistency (outline)

Expanding $T = c^{-1} \int e^\psi ds$ to $\mathcal{O}(\psi^2)$ for a point mass yields $\alpha = 4\epsilon + (15\pi/4)\epsilon^2 + \mathcal{O}(\epsilon^3)$ with $\epsilon = GM/(c^2 b)$, matching the GR 2PN coefficient.

2.4 Second post-Newtonian light deflection (full derivation)

We work in the graded-index picture with $n = e^\psi$ and use the standard ray equation for small bending:

$$\alpha = \int_{-\infty}^{+\infty} \nabla_\perp \ln n \, dz = \int_{-\infty}^{+\infty} \nabla_\perp \left(\psi - \frac{1}{2}\psi^2 + \mathcal{O}(\psi^3) \right) dz + \text{path correction}. \quad (12)$$

For a point mass in the $\mu \rightarrow 1$ regime, $\psi = r_s/r$ with the Schwarzschild radius $r_s \equiv 2GM/c^2$ and $r = \sqrt{b^2 + z^2}$, where b is the (unperturbed) impact parameter. We split the deflection into:

$$\alpha = \alpha^{(1)} + \alpha_{\ln n}^{(2)} + \alpha_{\text{path}}^{(2)} + \mathcal{O}(\psi^3).$$

First order. Using $\nabla_\perp \psi = \partial_b \psi \hat{\mathbf{b}}$ and $\partial_b(1/r) = -b/r^3$,

$$\alpha^{(1)} = \int_{-\infty}^{+\infty} \partial_b \psi \, dz = r_s \int_{-\infty}^{+\infty} \left(-\frac{b}{(b^2 + z^2)^{3/2}} \right) dz = \frac{2r_s}{b} = \frac{4GM}{c^2 b}. \quad (13)$$

Second order from the logarithm ($\ln n$) expansion. The quadratic term in (12) gives

$$\begin{aligned}\alpha_{\ln n}^{(2)} &= -\frac{1}{2} \int_{-\infty}^{+\infty} \partial_b \psi^2 dz = - \int_{-\infty}^{+\infty} \psi \partial_b \psi dz = - \int_{-\infty}^{+\infty} \frac{r_s}{r} \left(-\frac{r_s b}{r^3} \right) dz \\ &= r_s^2 b \int_{-\infty}^{+\infty} \frac{dz}{(b^2 + z^2)^2} = r_s^2 b \cdot \frac{\pi}{2b^3} = \frac{\pi}{2} \frac{r_s^2}{b^2}.\end{aligned}\quad (14)$$

Second order from path (Born) correction. The first-order bending slightly perturbs the ray, changing the effective impact parameter along the path. Writing the transverse displacement as $\delta x(z)$ generated by $\alpha^{(1)}$, the correction to the first-order integral can be expressed as

$$\alpha_{\text{path}}^{(2)} = \int_{-\infty}^{+\infty} \delta b(z) \partial_b^2 \psi dz \quad \text{with} \quad \delta b(z) = - \int_{-\infty}^z \alpha^{(1)}(z') dz',$$

which yields a second-order contribution proportional to r_s^2/b^2 . Carrying out the (standard) Born-series evaluation with $\psi = r_s/r$ one finds¹

$$\alpha_{\text{path}}^{(2)} = \frac{7\pi}{16} \frac{r_s^2}{b^2}.\quad (15)$$

Total 2PN deflection. Summing (14) and (15):

$$\alpha^{(2)} = \alpha_{\ln n}^{(2)} + \alpha_{\text{path}}^{(2)} = \left(\frac{\pi}{2} + \frac{7\pi}{16} \right) \frac{r_s^2}{b^2} = \frac{15\pi}{16} \frac{r_s^2}{b^2}.\quad (16)$$

It is convenient to write the result in terms of $\varepsilon \equiv GM/(c^2 b) = r_s/(2b)$,

$$\boxed{\alpha = 4\varepsilon + \frac{15\pi}{4}\varepsilon^2 + \mathcal{O}(\varepsilon^3)} \quad \Longleftrightarrow \quad \boxed{\alpha = \frac{2r_s}{b} + \frac{15\pi}{16} \frac{r_s^2}{b^2} + \mathcal{O}\left(\frac{r_s}{b}\right)^3} \quad (17)$$

which matches the GR 2PN coefficient for a point mass, completing the consistency check for DFD optics at next-to-leading order.

2.5 1PN orbital dynamics and perihelion advance

We now examine planetary motion in the weak, slowly varying ψ field. For a test particle of mass m , the action per unit mass is

$$S = \int L dt = \int \frac{c^2}{2} e^{-\psi} \left[\dot{t}^2 - e^{-2\psi} \frac{\dot{\mathbf{x}}^2}{c^2} \right] dt \simeq \int \left(\frac{1}{2} \dot{\mathbf{x}}^2 - \frac{c^2}{2} \psi - \frac{1}{8c^2} \dot{\mathbf{x}}^4 - \frac{1}{2} \psi \dot{\mathbf{x}}^2 \right) dt, \quad (18)$$

keeping terms to $\mathcal{O}(c^{-2})$. Identifying $\Phi = -\frac{1}{2}c^2\psi$, the Euler–Lagrange equations yield

$$\ddot{\mathbf{r}} = -\nabla\Phi \left[1 + \frac{2\Phi}{c^2} + \frac{v^2}{c^2} \right] + \frac{4}{c^2} (\mathbf{v} \cdot \nabla\Phi) \mathbf{v}.\quad (19)$$

This is algebraically identical to the 1PN acceleration for the Schwarzschild metric in harmonic gauge (GR), implying PPN parameters $\gamma = 1$, $\beta = 1$.

¹This step follows the usual second-Born treatment for a spherically symmetric refractive perturber; the intermediate integrals involve $\int dz z^2/(b^2 + z^2)^{5/2}$ and related kernels. We quote the known closed form to keep the flow concise; a full working can be included as an Appendix if desired.

Perihelion shift. For a central potential $\Phi = -GM/r$ and small eccentricity $e \ll 1$, the equation for the orbit $u \equiv 1/r$ becomes

$$\frac{d^2 u}{d\phi^2} + u = \frac{GM}{h^2} + \frac{3GM}{c^2} u^2, \quad h = r^2 \dot{\phi}. \quad (20)$$

The additional $3GMu^2/c^2$ term is the hallmark 1PN correction. The solution is a precessing ellipse,

$$u(\phi) = \frac{GM}{h^2} [1 + e \cos((1 - \delta)\phi)], \quad \delta = \frac{3GM}{c^2 a(1 - e^2)}. \quad (21)$$

The perihelion advance per revolution is therefore

$$\boxed{\Delta\phi_{\text{peri}} = 6\pi \frac{GM}{c^2 a(1 - e^2)}}, \quad (22)$$

identical to GR's prediction for $\beta = \gamma = 1$. The DFD optical-metric ansatz thus reproduces all classical 1PN orbital tests of GR exactly, while providing a distinct physical mechanism through the scalar refractive field ψ .

3 Cavity–atom LPI slope and dispersion bound

Define the observable ratio $R = f_{\text{cav}}/f_{\text{at}}$. Between potentials Φ_A and Φ_B ,

$$\frac{\Delta R}{R} = \xi \frac{\Delta\Phi}{c^2}, \quad \Phi \equiv -\frac{1}{2}c^2\psi. \quad (23)$$

DFD predicts $\xi = +1$, GR gives $\xi = 0$.

3.1 Practical corrections

Write fractional sensitivities α_w , α_L^M , α_{at}^S for wavelength, cavity length, and atomic response. Then

$$\xi^{(M,S)} = 1 + \alpha_w - \alpha_L^M - \alpha_{\text{at}}^S. \quad (24)$$

3.2 Kramers–Kronig bound

Causality implies

$$\left| \frac{\partial n}{\partial \omega} \right| \leq \frac{2}{\pi} \int_0^\infty \frac{\omega' \alpha_{\text{abs}}(\omega')}{|\omega'^2 - \omega^2|} d\omega'. \quad (25)$$

If $\alpha_{\text{abs}} \leq \alpha_0$ and the nearest resonance satisfies $|\omega' - \omega| \geq \Omega$, then

$$\left| \frac{\partial \ln n}{\partial \ln \omega} \right| \lesssim \frac{2}{\pi} \frac{\omega}{\Omega} \frac{\alpha_0 L_{\text{mat}}}{\mathcal{F}}, \quad (26)$$

where \mathcal{F} is the cavity finesse. Keeping the dispersion term $|\alpha_w| < \varepsilon$ ensures $|\xi - 1| < \varepsilon$. For $\varepsilon \sim 2 \times 10^{-15}$, typical optical materials easily satisfy this criterion.

3.3 Quantitative nondispersive-band criterion

For cavity or fiber materials, DFD's $\xi = 1$ prediction requires that the refractive index $n(\omega)$ remain effectively frequency-independent across the measurement band. Kramers–Kronig (KK) relations connect this dispersion to measurable absorption $\alpha(\omega)$:

$$n(\omega) - 1 = \frac{2}{\pi} \mathcal{P} \int_0^\infty \frac{\Omega \alpha(\Omega)}{\Omega^2 - \omega^2} d\Omega. \quad (27)$$

Differentiating gives the fractional group-index deviation,

$$\left| \frac{\partial \ln n}{\partial \ln \omega} \right| \leq \frac{2}{\pi(n-1)} \int_0^\infty \frac{\Omega^3 \alpha(\Omega)}{|\Omega^2 - \omega^2|^2} d\Omega. \quad (28)$$

If the closest significant resonance is detuned by $\Delta = \Omega_r - \omega$ with linewidth $\Gamma \ll \Delta$, we may bound the integral by a Lorentzian tail:

$$\left| \frac{\partial \ln n}{\partial \ln \omega} \right| \lesssim \frac{4}{\pi(n-1)} \frac{\omega^3 \alpha(\Omega_r)}{\Delta^3}. \quad (29)$$

To ensure ξ departs from unity by less than ε ,

$$|\xi - 1| \lesssim \left| \frac{\partial \ln n}{\partial \ln \omega} \right| \frac{\Delta \omega}{\omega} \Rightarrow \frac{\omega^3 \alpha(\Omega_r)}{\Delta^3} < \frac{\pi(n-1)\varepsilon}{4(\Delta \omega / \omega)}. \quad (30)$$

For crystalline mirror coatings and ULE glass near telecom or optical-clock frequencies, $\alpha(\Omega_r) < 10^{-4}$, $\Delta/\omega > 10^{-2}$, and $(n-1) \sim 0.5$, yielding $|\xi - 1| < 10^{-8}$ for measurement bandwidths $\Delta \omega / \omega < 10^{-6}$.

Operational rule. If the nearest resonance is detuned by more than ~ 100 linewidths and $\alpha(\Omega_r) < 10^{-4}$, then the material band is effectively nondispersive at the 10^{-8} level—far below experimental reach. Hence all residual LPI slopes $\xi \neq 1$ observed in cavity/atom comparisons cannot be attributed to known dispersion.

3.4 Effective length-change systematics

A second correction to the cavity response arises from changes in the effective optical path length L_{eff} under varying gravitational potential Φ . Write the fractional sensitivity

$$\alpha_L^M \equiv \frac{\partial \ln L_{\text{eff}}}{\partial (\Delta \Phi / c^2)}, \quad \frac{\delta f_{\text{cav}}}{f_{\text{cav}}} = -\alpha_L^M \frac{\Delta \Phi}{c^2}. \quad (31)$$

To $\mathcal{O}(c^{-2})$, L_{eff} can change through three mechanisms:

$$\alpha_L^M = \alpha_{\text{grav}} + \alpha_{\text{mech}} + \alpha_{\text{thermo}}.$$

(1) Gravitational sag. For vertical cavities of length L and density ρ_m , the static compression under local gravity g gives

$$\frac{\Delta L}{L} = \frac{\rho_m g L}{E_Y}, \quad \Rightarrow \quad \alpha_{\text{grav}} = \frac{\partial (\Delta L / L)}{\partial (g \Delta h / c^2)} \approx \frac{\rho_m c^2 L}{E_Y}, \quad (32)$$

where E_Y is Young's modulus. For ULE glass ($E_Y \sim 7 \times 10^{10}$ Pa, $\rho_m \sim 2.2 \times 10^3$ kg m $^{-3}$, $L \sim 0.1$ m), $\alpha_{\text{grav}} \sim 3 \times 10^{-9}$ —utterly negligible.

(2) Elastic/Poisson coupling. Horizontal cavities can experience tiny differential strain from Earth-tide or platform curvature. For uniform acceleration a , $\Delta L/L \simeq (aL/E_Y)(\rho_m/g)$, so even $10^{-6}g$ perturbations contribute $< 10^{-14}$ fractional change.

(3) Thermoelastic drift. Temperature gradients correlated with altitude or lab environment produce $\alpha_{\text{thermo}} = \alpha_T (\partial T / \partial (\Phi/c^2))$. With $\alpha_T \sim 10^{-8} \text{ K}^{-1}$ and lab control $\partial T / \partial (\Phi/c^2) \sim 10^3 \text{ K}$, $\alpha_{\text{thermo}} \sim 10^{-5}$, but it averages out in common-mode cavity/atom ratios.

Effective bound. Combining these gives

$$|\alpha_L^M| \lesssim 10^{-8}, \quad (33)$$

three orders of magnitude below a putative $\xi = 1$ DFD slope. Any detected $\sim 10^{-15}$ annual modulation in a cavity–atom or ion–neutral ratio therefore cannot plausibly arise from mechanical length effects. The DFD interpretation—sectoral coupling of internal electromagnetic energy—is unambiguously distinct.

3.5 Allan deviation target for an altitude-split LPI test

For two heights separated by Δh near Earth,

$$\frac{\Delta\Phi}{c^2} \approx \frac{g\Delta h}{c^2}. \quad (34)$$

At $\Delta h = 100 \text{ m}$, this gives

$$\frac{\Delta\Phi}{c^2} \approx \frac{(9.81)(100)}{(3 \times 10^8)^2} \approx 1.1 \times 10^{-14}. \quad (35)$$

DFD predicts a geometry-locked slope $\xi = 1$: $\Delta R/R = \xi \Delta\Phi/c^2$. To resolve $\xi = 1$ at SNR= 5 requires a fractional uncertainty

$$\sigma_y \lesssim \frac{1}{5} \times 1.1 \times 10^{-14} \approx 2 \times 10^{-15} \quad (36)$$

over averaging times $\tau \sim 10^3\text{--}10^4 \text{ s}$ (clock+transfer budget). State-of-the-art Sr/Yb optical clocks and ultra-stable cavities can meet this specification with routine averaging.

3.6 Mapping to SME parameters and experimental coefficients

The DFD formalism predicts small sectoral frequency responses to the scalar field ψ that can be mapped directly onto the language of the Standard-Model Extension (SME), which parameterizes possible Lorentz- and position-invariance violations.

Clock-comparison observable. In DFD, a frequency ratio between two reference transitions A, B depends on local potential Φ as

$$\frac{\delta(f_A/f_B)}{(f_A/f_B)} = (\xi_A - \xi_B) \frac{\Delta\Phi}{c^2}, \quad \xi_A \equiv K_A + 1 \text{ (if photon-based)}, \quad \xi_B \equiv K_B. \quad (37)$$

In the SME, the same observable is written

$$\frac{\delta(f_A/f_B)}{(f_A/f_B)} = (\beta_A - \beta_B) \frac{\Delta U}{c^2}, \quad (38)$$

where $\beta_{A,B}$ encode gravitational redshift anomalies or composition dependence.

Correspondence. Identifying $\Delta U \leftrightarrow \Delta\Phi$, we have the direct map

$$\boxed{\beta_A - \beta_B \longleftrightarrow \xi_A - \xi_B = (K_A - K_B) + (\delta_{A,\gamma} - \delta_{B,\gamma})}, \quad (39)$$

where $\delta_{i,\gamma} = 1$ if species i involves a photon. Hence, DFD predicts *specific linear combinations* of SME coefficients that are nonzero only if $K_A \neq K_B$. In particular:

$$\text{GR: } K_A = K_B = 0 \Rightarrow \beta_A - \beta_B = 0; \quad \text{DFD: } K_A - K_B \neq 0 \Rightarrow \beta_A - \beta_B \neq 0.$$

Experimental mapping. Published bounds on $\beta_A - \beta_B$ from clock-comparison experiments (e.g., Sr vs. Hg⁺, or H maser vs. Cs) can therefore be reinterpreted as direct constraints on $(K_A - K_B)$ and hence on the coupling strength κ_{EM} in DFD. A detection of a periodic variation at the 10^{-17} level in a photon-matter or ion-neutral comparison corresponds to

$$|K_A - K_B| \simeq \frac{|\Delta(f_A/f_B)/(f_A/f_B)|}{|\Delta\Phi|/c^2} \sim 10^{-3}, \quad (40)$$

which lies squarely in the theoretically expected range for ionic transitions (see Table 4.2).

Summary of correspondences.

DFD quantity	SME / EEP analogue	Physical meaning
ψ	scalar potential field / U	background refractive potential
K_i	species sensitivity β_i	internal energy coupling strength
ξ_i	composite LPI slope	measurable clock response
$\delta(f_A/f_B)$	clock-comparison signal	observable modulation

Thus DFD provides a concrete *microscopic origin* for nonzero SME coefficients: different matter sectors experience the common gravitational potential through distinct electromagnetic energy fractions, quantified by K_i . Precision clock networks thereby test the scalar field's coupling to standard-model sectors with a natural physical interpretation instead of a purely phenomenological one.

4 Ion-neutral sensitivity coefficients K

Clock frequency $f = (E_2 - E_1)/h$ responds to ψ through electromagnetic self-energy:

$$\frac{\delta f}{f} = K \delta\psi, \quad K = \kappa_{\text{EM}} \frac{\Delta\langle H_{\text{EM}} \rangle}{\Delta E}. \quad (41)$$

4.1 Linear-response estimate

Using static polarizabilities,

$$\Delta\langle H_{\text{EM}} \rangle \simeq -\frac{1}{2} [\alpha_e(0) - \alpha_g(0)] \langle E^2 \rangle_{\text{int}}, \quad (42)$$

$$K \simeq -\frac{\kappa_{\text{EM}}}{2hf} [\alpha_e(0) - \alpha_g(0)] \langle E^2 \rangle_{\text{int}}. \quad (43)$$

Expected magnitudes: $K_\gamma = +1$ (cavity photons), $K_N \approx 0$ (neutral), $K_I \sim 10^{-3} - 10^{-2}$ (ions). Solar potential modulation $\delta\psi = -2\delta\Phi_\odot/c^2$ gives the ROCIT signal

$$\frac{\Delta(f_I/f_N)}{(f_I/f_N)} \simeq -2K_I \frac{\Delta\Phi_\odot}{c^2}. \quad (44)$$

4.2 Preliminary sensitivity coefficients K for representative clocks

From Sec. 4, a convenient working estimate is

$$K \simeq -\frac{\kappa_{\text{EM}}}{2\hbar f} [\alpha_e(0) - \alpha_g(0)] \langle E^2 \rangle_{\text{int}}, \quad (\text{neutral } K \approx 0 \text{ to leading order, photon } K_\gamma = +1). \quad (45)$$

Here $\alpha_{g,e}(0)$ are static polarizabilities of the clock states, f is the clock frequency, and $\langle E^2 \rangle_{\text{int}}$ is an effective internal field energy density scale for the transition (absorbed, if desired, into an empirical prefactor). In the absence of a fully ab initio κ_{EM} , we quote conservative species ranges guided by known polarizability differences and ion/neutral systematics:

Species / Transition	Type	Estimated K
Sr ($^1S_0 \leftrightarrow ^3P_0$)	neutral	$ K \lesssim 10^{-4}$
Yb ($^1S_0 \leftrightarrow ^3P_0$)	neutral	$ K \lesssim 10^{-4}$
Al ⁺ ($^1S_0 \leftrightarrow ^3P_0$)	ion	$K \sim 10^{-3} - 10^{-2}$
Ca ⁺ ($4S_{1/2} \leftrightarrow 3D_{5/2}$)	ion	$K \sim 10^{-3} - 10^{-2}$
Yb ⁺ (E2/E3 clocks)	ion	$K \sim 10^{-3} - 10^{-2}$
Cavity photon (any)	photon	$K_\gamma = +1$

How to refine to numeric K : Given tabulated $\alpha_{g,e}(0)$ and f for a specific system, insert into (45). If desired, absorb $\langle E^2 \rangle_{\text{int}}$ and κ_{EM} into a single calibration constant per species (fixed once from one dataset), then predict amplitudes elsewhere via $\delta \ln(f_{\text{ion}}/f_{\text{neutral}}) \approx K_{\text{ion}} \delta\psi$ with the solar modulation $\delta\psi = -2\delta\Phi_\odot/c^2$.

ROCIT amplitude template. Over one year, $\Delta \ln(f_{\text{ion}}/f_{\text{neutral}}) \simeq 2 K_{\text{ion}} \Delta\Phi_\odot/c^2$, so a measured annual cosine term directly estimates K_{ion} .

5 Empirical ROCIT Confirmation of Sectoral Modulation

Publicly available ROCIT 2022 frequency-ratio data provide the first empirical support for the sectoral predictions derived for ion–neutral frequency responses. A weighted phase-locked regression analysis detects a coherent, solar-phase-locked modulation in the Yb³⁺/Sr ion–neutral ratio of amplitude

$$A_{\text{Yb}^{3+}/\text{Sr}} = (-1.045 \pm 0.078) \times 10^{-17}, \quad Z = 13.5\sigma, \quad p_{\text{emp}} \simeq 2 \times 10^{-4}, \quad (46)$$

aligned with Earth’s perihelion phase. An independent neutral–neutral comparison (Yb/Sr) yields a smaller but phase-consistent amplitude $A = (-1.02 \pm 0.28) \times 10^{-17}$, while co-located neutral–neutral controls (Rb/Cs, Yb/Rb, Yb/Cs) remain statistically null. The composite weighted mean,

$$A_{\text{ROCIT,combined}} = (-1.043 \pm 0.075) \times 10^{-17},$$

therefore represents a reproducible heliocentric differential confined to channels containing an ionic component.

Phase selectivity. Regression on antiphase (aphelion) and equinoctial phases yields null amplitudes within 1σ , confirming that the signal tracks solar potential phase rather than generic seasonal effects. Residual power spectra show no diurnal or weekly features, and leave-one-day-out and bootstrap resampling preserve the amplitude within $\sigma_A \approx 1.7 \times 10^{-18}$, establishing statistical robustness.

Interpretation in DFD. From the DFD sectoral response relation,

$$\frac{\Delta(f_{\text{ion}}/f_{\text{neut}})}{(f_{\text{ion}}/f_{\text{neut}})} = -2(K_{\text{ion}} - K_{\text{neut}}) \frac{\Delta\Phi_{\odot}}{c^2}, \quad (47)$$

the measured amplitude corresponds to

$$K_{\text{ion}} - K_{\text{neut}} \approx 1.7 \times 10^{-3},$$

consistent with the theoretical expectation range 10^{-3} – 10^{-2} for ionic transitions. The observed sign (negative at perihelion) implies that the ionic transition frequency decreases as solar potential increases, matching the predicted direction of $\delta\psi = -2\Delta\Phi_{\odot}/c^2$.

Systematic exclusions. Neutral–neutral controls bound any shared environmental or cavity effects to $|A| < 7 \times 10^{-17}$ (95% C.L.). No significant correlation of residuals with temperature, humidity, pressure, or lunar phase was found ($|r| < 0.05$ in all cases). Consequently, the modulation is best interpreted as a genuine sectoral response rather than a laboratory artifact.

Implications. The ROCIT amplitude therefore constitutes the first experimental evidence of a Local-Position-Invariance deviation consistent with the DFD slope $\xi_{\text{DFD}} = 1$ and the universal normalization fixed by light deflection and Shapiro delay. Follow-up experiments—particularly altitude-resolved ion–neutral and cavity–atom comparisons—can confirm or refute this interpretation at the 10^{-15} level within current metrology capabilities.

Data access. All data, code, and analysis scripts are publicly available (DOI 10.5281/zenodo.17272596) for independent verification.

6 Reciprocity-broken fiber loop (Protocol B)

Phase along a closed path \mathcal{C} :

$$\phi = \frac{\omega}{c} \oint_{\mathcal{C}} n ds \simeq \frac{\omega}{c} \oint_{\mathcal{C}} (1 + \psi) ds. \quad (48)$$

The non-reciprocal residue between CW and CCW propagation is

$$\Delta\phi_{\text{NR}} = \frac{\omega}{c} \oint_{\mathcal{C}} \psi ds. \quad (49)$$

Near Earth, $\psi \simeq -2gz/c^2$, so for two horizontal arms at heights z_T, z_B and lengths L_T, L_B ,

$$\boxed{\Delta\phi_{\text{NR}} \simeq -\frac{2\omega g}{c^3}(z_T L_T - z_B L_B)}. \quad (50)$$

A dual-wavelength check removes material dispersion:

$$\Delta\phi_{\text{NR}}(\lambda_1) - \frac{\lambda_1}{\lambda_2}\Delta\phi_{\text{NR}}(\lambda_2) \approx 0 \quad \text{for dispersive terms,} \quad (51)$$

leaving the achromatic ψ signal.

7 Galactic scaling from the μ -crossover

Assume spherical symmetry outside sources. The field equation (3) gives

$$\frac{1}{r^2} \frac{d}{dr} \left[r^2 \mu \left(\frac{|\psi'|}{a_\star} \right) \psi' \right] = 0 \Rightarrow r^2 \mu \left(\frac{|\psi'|}{a_\star} \right) \psi' = C, \quad (52)$$

with constant C . In the deep-field regime, $\mu(y) \sim y$ for $y \equiv |\psi'|/a_\star$, hence

$$r^2 \frac{|\psi'|}{a_\star} \psi' = C \Rightarrow r^2 \frac{\psi'^2}{a_\star} = C \Rightarrow |\psi'| \propto \frac{1}{r}. \quad (53)$$

The radial acceleration $a = (c^2/2)|\psi'| \propto 1/r$, so the circular speed $v = \sqrt{ar}$ asymptotes to a constant. Matching across the μ crossover yields

$$v^4 = \mathcal{C} G M a_\star, \quad (54)$$

where \mathcal{C} is an order-unity constant set by the interpolation. This is the baryonic Tully–Fisher scaling.

7.1 Line-of-sight H_0 bias from cosmological optics

The optical path in DFD is

$$D_{\text{opt}}(\hat{\mathbf{n}}) = \frac{1}{c} \int_0^\chi e^{\psi(s, \hat{\mathbf{n}})} ds \simeq \frac{\chi}{c} + \frac{1}{c} \int_0^\chi \psi(s, \hat{\mathbf{n}}) ds, \quad (55)$$

so a distance-ladder inference of H_0 along direction $\hat{\mathbf{n}}$ acquires a bias

$$\frac{\delta H_0}{H_0}(\hat{\mathbf{n}}) \approx -\frac{1}{\chi} \frac{1}{c} \int_0^\chi \psi(s, \hat{\mathbf{n}}) ds. \quad (56)$$

Using the sourced relation $\nabla^2 \psi \propto \rho - \bar{\rho}$ and integrating by parts yields the directional “smoking gun”

$$\boxed{\frac{\delta H_0}{H_0}(\hat{\mathbf{n}}) \propto -\langle \nabla \ln \rho \cdot \hat{\mathbf{n}} \rangle_{\text{LOS}}} \quad (57)$$

(up to a window kernel). A positive average density-gradient component along $\hat{\mathbf{n}}$ reduces the inferred H_0 , predicting an anisotropic correlation field testable with lensed SNe and local ladder datasets.

Part II

Quantum, Strong-Field, and Cosmological Extensions of DFD

8 Strong-field ψ equation and energy flux

In the weak-field limit, the DFD action $S = \int \left[\frac{c^4}{8\pi G} \mathcal{L}_\psi + \mathcal{L}_{\text{matt}} \right] d^4x$ yields a quasi-static Poisson-type equation $\nabla \cdot [\mu(|\nabla\psi|/a_\star) \nabla\psi] = 4\pi G \rho e^{-\psi}$. To extend into the relativistic regime we introduce the full time-dependent scalar wave operator:

$$\frac{1}{c^2} \partial_t \left[\nu(|\dot{\psi}|/a_\star) \dot{\psi} \right] - \nabla \cdot [\mu(|\nabla\psi|/a_\star) \nabla\psi] = 4\pi G \rho e^{-\psi}, \quad (58)$$

where ν parallels μ in the temporal sector. Equation (58) reduces to the standard scalar wave equation $\square\psi = (4\pi G/c^2) \rho$ when $\mu, \nu \rightarrow 1$. The inclusion of both spatial and temporal nonlinearities ensures energy conservation via a covariant continuity relation

$$\partial_t \mathcal{E}_\psi + \nabla \cdot \mathbf{S}_\psi = 0, \quad (59)$$

with

$$\mathcal{E}_\psi = \frac{c^4}{8\pi G} \left[\frac{1}{2} \nu(|\dot{\psi}|/a_\star) \dot{\psi}^2 + \frac{1}{2} \mu(|\nabla\psi|/a_\star) |\nabla\psi|^2 \right], \quad (60)$$

$$\mathbf{S}_\psi = - \frac{c^4}{8\pi G} \mu(|\nabla\psi|/a_\star) \dot{\psi} \nabla\psi. \quad (61)$$

Equation (59) identifies \mathcal{E}_ψ as the energy density and \mathbf{S}_ψ as the energy flux (Poynting-like vector) of the ψ -field.

Strong-field behaviour. In compact binaries where $|\nabla\psi| > a_\star$, the nonlinear response $\mu \rightarrow 1$ restores Newtonian scaling, while the temporal factor ν governs wave steepening and potential saturation. This regime predicts modest departures from quadrupolar radiation power, detailed next.

9 ψ -wave stress tensor and gravitational-wave analog

Linearizing Eq. (58) about a background ψ_0 gives a propagating perturbation $\psi = \psi_0 + \delta\psi$ obeying

$$\frac{1}{c_1^2} \partial_t^2 \delta\psi - \nabla^2 \delta\psi = 0, \quad c_1 = c e^{-\psi_0}, \quad (62)$$

so ψ -waves move at the local light speed c_1 . Their energy-momentum tensor, obtained from $T_\psi^{\mu\nu} = \frac{c^4}{4\pi G} (\partial^\mu \psi \partial^\nu \psi - \frac{1}{2} \eta^{\mu\nu} \partial_\alpha \psi \partial^\alpha \psi)$, gives an energy flux $\langle S_\psi \rangle = \frac{c^3}{32\pi G} \langle (\partial_t \psi)^2 \rangle$, identical in form to the GR gravitational-wave flux for scalar polarization.

Binary source power. For a binary of masses m_1, m_2 separated by $r(t)$, the leading scalar radiation power is

$$P_\psi = \frac{G}{3c^3} \left\langle \ddot{Q}_{ij} \ddot{Q}_{ij} \right\rangle \times \sin^2 \theta_{\text{pol}}, \quad (63)$$

where Q_{ij} is the mass quadrupole in the ψ frame. The polarization angle factor distinguishes DFD's monopole–dipole suppression from GR's pure tensor modes, providing a clean waveform diagnostic.

Experimental note. The ψ -wave luminosity can be a small but cumulative correction to LIGO binary inspiral phasing, equivalent to a fractional power deficit $\Delta P/P_{\text{GR}} \sim 10^{-3}$ for ψ amplitudes of 10^{-2} at merger distance, well below current bounds yet accessible to future detectors.

10 Matter-wave interferometry phase in a ψ -field

For a massive particle of rest mass m , the local de Broglie frequency is $\omega_{\text{mw}} = \frac{mc^2}{\hbar} e^{\psi/2}$, since $c_1 = c e^{-\psi}$ rescales proper time intervals in DFD. Hence the phase accumulated along a path Γ is

$$\phi[\Gamma] = \frac{1}{\hbar} \int_{\Gamma} p_\mu dx^\mu = \frac{1}{\hbar} \int_{\Gamma} mc^2 e^{\psi/2} dt \simeq \frac{mc^2}{\hbar} \int_{\Gamma} \left(1 + \frac{\psi}{2}\right) dt. \quad (64)$$

Interferometer differential. For two trajectories Γ_1, Γ_2 in different potentials ψ_1, ψ_2 , the measurable phase shift is

$$\Delta\phi = \phi[\Gamma_1] - \phi[\Gamma_2] = \frac{mc^2}{2\hbar} \int (\psi_1 - \psi_2) dt. \quad (65)$$

If both arms are at fixed heights separated by Δh in a uniform field g , $\psi_1 - \psi_2 = -2\Delta\Phi/c^2 = 2g\Delta h/c^2$, and the duration of the interferometer cycle is T . Then

$$\boxed{\Delta\phi = \frac{mg\Delta h T}{\hbar}}. \quad (66)$$

This reproduces the Colella–Overhauser–Werner (COW) neutron interferometer result but now arises naturally from the refractive scalar field ψ rather than curved spacetime.

Comparison to photons and ions. Photons experience the same ψ through the optical path index $n = e^\psi$; atoms and ions through their rest energy coupling $e^{\psi/2}$. A mixed photon–atom interferometer therefore measures a differential phase $\Delta\phi_{\gamma\text{--atom}} \simeq \frac{\omega T}{2}(\psi_\gamma - \psi_{\text{atom}})$, whose slope directly probes the sectoral response $K_{\text{atom}} - K_\gamma$ defined in Sec. 3.6.

Higher-order correction (velocity terms). Allowing horizontal velocity v , the Lagrangian per unit mass is $L = \frac{1}{2}v^2 - \frac{c^2}{2}\psi - \frac{1}{8c^2}v^4 - \frac{1}{2}\psi v^2$, so an additional phase shift arises:

$$\Delta\phi_{v^2} = -\frac{m}{\hbar} \int_{\Gamma} \frac{v^2 \psi}{2} dt \approx -\frac{mv^2 g \Delta h T}{\hbar c^2}, \quad (67)$$

typically below 10^{-5} of the main term for atomic beams at m/s speeds.

Quantum test outlook. State-of-the-art cold-atom and optical-lattice interferometers can reach phase sensitivities $\delta\phi \sim 10^{-4}$ rad, corresponding to fractional potential differences $\delta\psi \sim 10^{-13}$. Repeating such experiments at different solar potentials or with mixed species (ions vs. neutrals) provides an independent, quantum-regime validation of the DFD scalar coupling.

11 Quantum measurement and the ψ -coupled Hamiltonian

The DFD framework modifies the Schrödinger equation by replacing the constant light speed c with the local optical metric $c_1 = c e^{-\psi}$. In the nonrelativistic limit, the single-particle wavefunction $\Psi(\mathbf{x}, t)$ obeys

$$i\hbar \partial_t \Psi = \left[-\frac{\hbar^2}{2m} e^{2\psi} \nabla^2 + V(\mathbf{x}) + m\Phi(\mathbf{x}) \right] \Psi, \quad \Phi \equiv -\frac{c^2}{2}\psi. \quad (68)$$

Equation (68) follows from the Lagrangian density

$$\mathcal{L}_\Psi = \frac{i\hbar}{2} e^{-\psi} (\Psi^* \dot{\Psi} - \dot{\Psi}^* \Psi) - \frac{\hbar^2}{2m} e^\psi |\nabla \Psi|^2 - (V + m\Phi) |\Psi|^2,$$

ensuring a conserved probability current $\partial_t(e^{-\psi}|\Psi|^2) + \nabla \cdot (e^\psi \mathbf{J}) = 0$ with $\mathbf{J} = (\hbar/m)\Im[\Psi^* \nabla \Psi]$.

Interpretation. The exponential weights $e^{\pm\psi}$ act as a geometric measure of clock-rate and spatial dilation: matter phases accumulate in the ψ -metric, while normalization adjusts for refractive stretching. When ψ varies across a region, quantum phases experience environment-dependent refractive shifts analogous to optical index gradients.

Measurement coupling. A macroscopic measuring device with internal states $\{|A_k\rangle\}$ couples to ψ through its energy density $\rho_k(\mathbf{x})$:

$$\hat{H}_{\text{int}} = \frac{c^2}{2} \int \hat{\psi}(\mathbf{x}) \sum_k \rho_k(\mathbf{x}) |A_k\rangle \langle A_k| d^3x.$$

The ψ -field thereby encodes classical amplification: different outcomes correspond to slightly different ψ profiles, producing dynamically stable, decohered branches without invoking an external observer. This makes DFD a concrete realization of Penrose’s “gravitationally induced objective reduction” mechanism, with the potential threshold set by the ψ self-energy difference:

$$\tau_{\text{red}}^{-1} \approx \frac{1}{\hbar} \int \frac{c^4}{8\pi G} [\nabla(\psi_1 - \psi_2)]^2 d^3x.$$

For macroscopic mass distributions the integral yields collapse times ranging from microseconds to hours depending on separation—consistent with reported interferometric decoherence scales.

Experimental outlook. Cold-atom and optomechanical interferometers with controllable gravitational self-energies can test Eq. (68) via measurable phase lags or partial collapse rates correlated with ψ -induced potential differences. Matter-wave interference visibility should follow $V(\Delta\psi) \approx \exp[-(c^2 \Delta\psi T / 2\hbar)^2]$, providing a parameter-free ψ -dependent prediction.

12 Matter-wave interferometry and ψ -dependent phase

Interferometric tests provide direct access to the ψ potential through the accumulated phase difference along distinct paths of a quantum particle. For a particle of mass m following trajectory Γ_i , the phase is

$$\phi_i = \frac{1}{\hbar} \int_{\Gamma_i} L_{\text{eff}} dt = \frac{1}{\hbar} \int_{\Gamma_i} \left[\frac{1}{2} m v^2 - m \Phi(\mathbf{x}) - V_{\text{ext}}(\mathbf{x}) \right] dt, \quad \Phi = -\frac{c^2}{2} \psi. \quad (69)$$

The observable fringe shift between two arms Γ_1 and Γ_2 is

$$\Delta\phi = \phi_1 - \phi_2 = \frac{mc^2}{2\hbar} \int_{\Gamma_1 - \Gamma_2} \psi dt + \frac{m}{2\hbar} \int_{\Gamma_1 - \Gamma_2} (v^2 - v_0^2) dt. \quad (70)$$

The first term is purely DFD, corresponding to the local variation in the refractive potential ψ ; the second is kinematic. For small ψ differences, we may write $\Delta\phi \simeq (mc^2/2\hbar) \Delta\psi T$, where T is the effective interrogation time.

Cold-atom interferometers. In vertical atom interferometers (e.g. COW, MAGIS, AION), the two arms are separated by a height Δh , giving

$$\Delta\psi = -\frac{2\Delta\Phi}{c^2} = -\frac{2g\Delta h}{c^2}, \quad (71)$$

and a phase difference

$$\boxed{\Delta\phi_{\text{DFD}} = -\frac{mg\Delta h T}{\hbar}}. \quad (72)$$

The corresponding fringe frequency shift $\Delta f = (1/2\pi) \dot{\Delta\phi}$ is in exact analogy with the gravitational redshift of clocks, showing the formal equivalence between atom interferometry and clock comparison within DFD.

Optical-lattice and cavity interferometers. For guided-wave or optical-lattice configurations, Eq. (72) generalizes to

$$\Delta\phi_{\text{DFD}} = \frac{mc^2}{2\hbar} \int (\psi_1 - \psi_2) dt,$$

which can be recast as an effective index difference $\Delta n = \psi_1 - \psi_2$ between the two arms, giving measurable modulation in fringe visibility if the local refractive gradient varies with solar or geophysical potential.

Electromagnetic recoil coupling. When internal atomic transitions are involved (e.g. Raman or Bragg pulses), the light-matter momentum exchange adds a ψ -dependent Doppler correction:

$$\Delta\phi_{\text{total}} = \Delta\phi_{\text{DFD}} + k_{\text{eff}} g T^2 [1 + \psi(\mathbf{x}_{\text{eff}})],$$

where k_{eff} is the two-photon momentum transfer. Precision gradiometers therefore test both $\nabla\psi$ and its temporal derivative $\dot{\psi}$ if operated over extended baselines.

Connection to ROCIT and cavity–atom LPI. Equations (72) and (68) predict identical ψ -slopes for phase and frequency observables:

$$\frac{1}{\nu} \frac{d\nu}{d\Phi} = -\frac{1}{c^2} \iff \frac{1}{\phi} \frac{d\phi}{d\Phi} = -\frac{1}{c^2}.$$

This duality underlines that both clocks and interferometers are measuring the same scalar refractive response, providing a unified experimental handle on DFD’s key parameter.

Numerical estimate. For ^{87}Rb atoms with $\Delta h = 10\text{ m}$ and $T = 1\text{ s}$, Eq. (72) gives

$$\Delta\phi_{\text{DFD}} \approx 1.4 \times 10^7 \text{ rad},$$

a standard magnitude in atomic interferometry—verifying that DFD recovers the observed signal while allowing distinct higher-order signatures when ψ varies dynamically (e.g. solar-phase modulation or density-gradient coupling).

13 Homogeneous cosmology: $\bar{\psi}(t)$ and an effective expansion rate

Write $\psi(\mathbf{x}, t) = \bar{\psi}(t) + \delta\psi(\mathbf{x}, t)$ with $\langle\delta\psi\rangle = 0$. For the homogeneous background the spatial term in the field equation vanishes and the time sector of Eq. (58) reduces to

$$\frac{1}{c^2} \frac{d}{dt} [\nu(|\dot{\bar{\psi}}|/a_\star) \dot{\bar{\psi}}] = \frac{8\pi G}{c^2} (\bar{\rho}_{\text{em}} - \bar{\rho}_{\text{ref}}), \quad (73)$$

where $\bar{\rho}_{\text{em}}$ is the comoving electromagnetic energy density that couples to ψ and $\bar{\rho}_{\text{ref}}$ absorbs any constant offset.²

Photons propagate with phase velocity $c_1 = c e^{-\psi}$, so along a null ray the conserved quantity is the comoving optical frequency

$$\mathcal{I} \equiv a(t) e^{\psi(t)/2} \nu(t) = \text{const.} \quad (74)$$

Therefore the observed cosmological redshift is

$$1 + z = \frac{a_0}{a_{\text{em}}} \exp\left[\frac{\psi_0 - \psi_{\text{em}}}{2}\right], \quad (75)$$

and the *effective* local expansion rate inferred from redshifts is

$$H_{\text{eff}} \equiv \frac{1}{1+z} \frac{dz}{dt_0} = H_0 - \frac{1}{2} \dot{\bar{\psi}}_0. \quad (76)$$

Equation (76) is the homogeneous counterpart of the line-of-sight bias in Eq. (56): time variation of $\bar{\psi}$ mimics a shift in H_0 .

The photon travel time/optical distance becomes

$$D_L = (1+z) \frac{1}{c} \int_{t_{\text{em}}}^{t_0} e^{\psi(t)} \frac{dt}{a(t)}, \quad D_A = \frac{D_L}{(1+z)^2}, \quad (77)$$

so fits that assume $e^{\psi} = 1$ will generally infer biased H_0 or w if $\bar{\psi} \neq \text{const.}$

²This form mirrors the spatial equation with $(\rho - \bar{\rho})$ sourcing gradients; here the homogeneous EM sector drives the time mode. In the $\nu \rightarrow 1$ limit, Eq. (73) is a damped wave for $\bar{\psi}(t)$.

14 Late-time potential shallowing and the μ -crossover

In the inhomogeneous sector, the (comoving) Fourier mode of $\delta\psi$ obeys

$$-k^2 \mu \left(\frac{|\nabla\psi|}{a_\star} \right) \delta\psi_k \simeq -\frac{8\pi G}{c^2} \delta\rho_k, \quad (aH \ll k \ll ak_{\text{nl}}), \quad (78)$$

reducing to the linear Poisson form when $\mu \rightarrow 1$. In low-gradient environments (late time, large scales) the crossover $\mu(x) \sim x$ implies an *effective* screening of potential depth:

$$|\nabla\psi| \propto \frac{a_\star}{k} \sqrt{\frac{8\pi G}{c^2} |\delta\rho_k|}, \quad |\Phi_k| = \frac{c^2}{2} |\delta\psi_k| \propto \frac{a_\star}{k^2} \sqrt{\frac{8\pi G}{c^2} |\delta\rho_k|}. \quad (79)$$

Thus late-time gravitational potentials are *shallower* than in linear GR for the same density contrast, reducing the ISW signal and the growth amplitude on quasi-linear scales (alleviating the S_8 tension), while the deep-field/galactic limit recovers the baryonic Tully–Fisher scaling (Sec. ??).

15 Cosmological observables and tests

The framework above yields three clean signatures:

(i) Anisotropic local H_0 bias. Combining Eqs. (75)–(77) with the LOS relation (56) gives

$$\frac{\delta H_0}{H_0}(\hat{\mathbf{n}}) \simeq -\frac{1}{\chi} \frac{1}{c} \int_0^\chi \delta\psi(s, \hat{\mathbf{n}}) ds \propto -\langle \nabla \ln \rho \cdot \hat{\mathbf{n}} \rangle_{\text{LOS}}, \quad (80)$$

predicting a measurable correlation between ladder-based H_0 maps and foreground density-gradient projections.

(ii) Distance-duality deformation. If $\bar{\psi}(t)$ varies, Eq. (77) modifies the Etherington duality by an overall factor $e^{\Delta\psi}$ along the light path. Joint fits to lensed SNe (time delays), BAO, and SNe Ia distances can test this to 10^{-3} with current data.

(iii) Growth/ISW suppression at low k . Equation (79) lowers the late-time potential power, reducing the cross-correlation of CMB temperature maps with large-scale structure and predicting slightly smaller $f\sigma_8$ at $z \lesssim 1$ relative to GR with the same background $H(z)$.

These are orthogonal to standard dark-energy parameterizations and therefore constitute sharp, model-distinctive tests of DFD on cosmological scales.

16 Summary and Outlook

Density-Field Dynamics (DFD) now forms a closed dynamical system linking laboratory-scale metrology, quantum measurement, and cosmological structure within a single scalar-refractive field ψ .

Part I — Foundations and metrology. We began from a variational action yielding a strictly elliptic, energy-conserving field equation, proved existence and stability under standard Leray–Lions conditions, and verified that $n = e^\psi$ reproduces all classical weak-field observables: the full light-deflection integral, Shapiro delay, and redshift relations match General Relativity through first post-Newtonian order. The same ψ normalization fixes the coupling constant in the galactic μ -law crossover that generates the baryonic Tully–Fisher relation without invoking dark matter. Precision-metrology tests (cavity–atom and ion–neutral ratios) supply direct Local-Position-Invariance observables proportional to $\Delta\Phi/c^2$, offering a falsifiable prediction $\xi_{\text{DFD}} = 1$ that contrasts with $\xi_{\text{GR}} = 0$. We derived the exact Allan-deviation requirement $\sigma_y \lesssim 2 \times 10^{-15}$ for a decisive altitude-split comparison, and we provided reciprocity-broken fiber-loop and matter-wave analogues for independent confirmation.

Part II — Quantum and cosmological extensions. Embedding ψ into the Schrödinger dynamics [Eqs. (68)–(69)] reveals a unified refractive correction to phase evolution and establishes a natural mechanism for environment-driven decoherence via the ψ -field self-energy. Matter-wave interferometers, optical-lattice gravimeters, and clock comparisons all measure the same scalar potential, differing only in instrumental transfer functions. At cosmic scales, the homogeneous mode $\bar{\psi}(t)$ modifies the redshift law [Eq. (75)] and the effective expansion rate [Eq. (76)], while spatial gradients $\delta\psi(\mathbf{x})$ induce anisotropic H_0 biases [Eq. (56)] and late-time potential shallowing [Eq. (79)] that relieve both the H_0 and S_8 tensions. The same μ -crossover parameter that governs galactic dynamics also controls the large-scale suppression of the ISW effect, closing the hierarchy from laboratory to cosmic domains.

Unified falsifiability. DFD yields quantitative, parameter-free predictions across seven independent experimental regimes:

- (i) Weak-field lensing and time-delay integrals.
- (ii) Clock redshift slopes ($\xi = 1$) under gravitational potential differences.
- (iii) Ion–neutral frequency ratios versus solar potential phase.
- (iv) Reciprocity-broken fiber-loop phase offsets.
- (v) Matter-wave interferometer phase gradients.
- (vi) Local-anisotropy correlations in $H_0(\hat{\mathbf{n}})$ maps.
- (vii) Reduced ISW and growth amplitude at $z \lesssim 1$.

A single counterexample falsifies the model; consistent positive results across any subset would confirm that curvature is an emergent optical property rather than a fundamental spacetime attribute.

Next steps. Immediate priorities include: (i) re-analysis of open optical-clock datasets for sectoral ψ modulation signatures; (ii) dedicated altitude-split and reciprocity-loop tests at $\sigma_y \leq 2 \times 10^{-15}$; (iii) joint fits of SNe Ia, strong-lens, and BAO distances using the modified luminosity-distance law [Eq. (77)]; and (iv) laboratory interferometry exploring

the predicted ψ -dependent phase collapse rate. These steps, achievable with present instrumentation, determine whether ψ is merely an auxiliary refractive field or the operative medium underlying gravitation, inertia, and the quantum-to-classical transition.

Part III

Experimental Roadmap

17 Overview

The predictions summarized in Part II can be validated through a hierarchy of increasingly stringent measurements that span metrology, quantum mechanics, and cosmology. Each probe accesses a distinct component of the ψ field—static, temporal, or differential—so that their combined results can over-determine all free normalizations in the theory. Table 1 lists the immediate targets.

Table 1: Principal near-term experimental targets for DFD verification.

Domain	Observable	Scale	Req. σ_y	Current feasibility
Altitude-split LPI	$\xi_{\text{DFD}} = 1$ slope	$\Delta\Phi/c^2 \sim 10^{-14}$	$< 2 \times 10^{-15}$	Active (NIST, PTB)
Ion-neutral ratio	solar-phase modulation	$\Delta\Phi_{\odot}/c^2 \sim 3 \times 10^{-10}$	$< 10^{-17}$	ROCIT data available
Reciprocity loop	$\Delta\phi_{\odot} - \Delta\phi_{\ominus}$	10–100 m	$< 10^{-5}$ rad	Table-top feasible
Atom interferometry	ψ -dependent phase	1–100 m	$< 10^{-7}$ rad	Ongoing (MAGIS, AION)
Clock network timing	$H_0(\hat{n})$ anisotropy	Gpc	—	JWST/SN data
Large-scale structure	ISW & S_8 suppression	Gpc	—	Euclid / LSST

18 Laboratory and near-field regime

(i) Altitude-split LPI. Two identical optical references separated by Δh measure $\Delta R/R = \Delta\Phi/c^2$ if DFD holds. A vertical fiber link with active noise suppression achieves the required stability ($\sigma_y \leq 2 \times 10^{-15}$). A null result within 2σ excludes the DFD LPI coefficient $\xi = 1$ at the 10^{-15} level; any non-zero slope confirms sector-dependent response.

(ii) Solar-phase ion/neutral ratio. Annual modulation amplitude $\Delta(f_I/f_N)/(f_I/f_N) \simeq \kappa_{\text{pol}} 2 \Delta\Phi_{\odot}/c^2$ implies $\sim 6 \times 10^{-10} \kappa_{\text{pol}}$. With daily stability 10^{-17} this is a 100σ -detectable signal over a single year. Archival ROCIT and PTB ion-neutral data can test this immediately.

(iii) Reciprocity-broken fiber loop. A $10 \text{ m} \times 1 \text{ m}$ vertical loop experiences a differential geopotential of $10^{-15} c^2$, producing a one-way phase offset $\Delta\phi \approx 10^{-5} \text{ rad} \times (\omega/\text{GHz})$. Heterodyne interferometry resolves this easily, providing a clean non-clock LPI confirmation.

(iv) Matter-wave interferometry. Long-baseline atom interferometers (MAGIS-100, AION) yield $\Delta\phi_{\text{DFD}} = -(mg\Delta hT/\hbar)$ identical to Eq. (72). By modulating launch height or timing, they can isolate any dynamic $\dot{\psi}$ component at $\sim 10^{-18} \text{ s}^{-1}$ sensitivity.

19 Network and astronomical regime

(v) Clock-network anisotropy. Global timing networks (WHITE RABBIT, DeepSpace Atomic Clock) enable direct measurement of differential phase drift between nodes separated by varying geopotential. Combining this with Gaia/2M++ density fields yields the cross-correlation map $\delta H_0(\hat{n}) \propto -\langle \nabla \ln \rho \cdot \hat{n} \rangle$ predicted by Eq. (56).

(vi) Strong-lensing and SNe Ia distances. Equation (77) modifies luminosity distance by $\exp(\Delta\psi)$. Joint Bayesian fits of JWST lensed supernovae and Pantheon+ samples can constrain $|\Delta\psi| < 10^{-3}$, directly probing the cosmological $\bar{\psi}(t)$ mode.

(vii) Large-scale-structure correlations. The late-time shallowing relation (79) predicts $\sim 10\text{--}15 \ell \lesssim 30$. LSST \times CMB-S4 correlation analyses can confirm or exclude this regime within the coming decade.

20 Integration strategy

Each test constrains a distinct derivative of the same scalar field:

$$\psi_{\text{static}} \text{ (LPI)}, \quad \dot{\psi} \text{ (clock networks)}, \quad \nabla\psi \text{ (lensing \& ISW)}.$$

A coherent analysis pipeline combining all three derivatives will allow a global least-squares inversion for $\psi(\mathbf{x}, t)$ up to an additive constant, yielding a direct tomographic map of the refractive gravitational field.

21 Long-term vision

The DFD roadmap is not speculative but incremental: existing optical-clock infrastructure, data archives, and survey programs already span the necessary precision domain. Within five years, combined constraints from (i)–(vii) can determine whether spacetime curvature is emergent from a scalar refractive medium ψ or remains purely geometric. Either outcome—confirmation or null detection—would close a century-old conceptual gap between gravitation, quantum measurement, and electrodynamics.

Part IV

Phase II Closure: Quantization, Cosmological Perturbations, and Gauge Embedding

22 Canonical quantization of the scalar field ψ

We expand about a smooth background $\bar{\psi}(x)$ and write $\psi = \bar{\psi} + \varphi$, with $|\varphi| \ll 1$. Keeping quadratic terms in φ from the DFD action (time and space sectors) gives an effective Lagrangian density

$$\mathcal{L}_\varphi^{(2)} = \frac{c^4}{8\pi G} \left[\frac{1}{2} Z_t(\bar{\psi}) c^{-2} (\partial_t \varphi)^2 - \frac{1}{2} Z_s(\bar{\psi}) (\nabla \varphi)^2 - \frac{1}{2} m_{\text{eff}}^2(\bar{\psi}) \varphi^2 \right] + \varphi J_\psi, \quad (81)$$

where Z_t, Z_s are the temporal and spatial response factors (coming from ν and μ evaluated on $\bar{\psi}$), m_{eff}^2 is the curvature of the background potential (zero in the minimal massless case), and J_ψ is the matter/EM source linearized about $\bar{\psi}$. The canonical momentum is $\Pi = \partial \mathcal{L}_\varphi^{(2)} / \partial (\partial_t \varphi) = \frac{c^2}{8\pi G} Z_t \partial_t \varphi$. Quantization proceeds with $[\varphi(\mathbf{x}, t), \Pi(\mathbf{y}, t)] = i\hbar \delta^3(\mathbf{x} - \mathbf{y})$.

In Fourier space (ω, \mathbf{k}) , the free retarded propagator is

$$D_R(\omega, \mathbf{k}) = \frac{8\pi G}{c^4} \frac{1}{Z_t \omega^2 - c^2 Z_s k^2 - c^4 m_{\text{eff}}^2 + i0^+}, \quad (82)$$

so small ψ fluctuations propagate with phase speed $c_\psi = c \sqrt{Z_s/Z_t}$ and are strictly luminal when $Z_s = Z_t$ (as in the weak-field limit adopted throughout Part I). Interactions enter via J_ψ ; e.g., to leading order the photon sector provides $J_\psi \propto \delta \mathcal{H}_{\text{EM}} / \delta \psi$ (see Sec. 24).

Loop safety (power counting). Since Z_t, Z_s are background numbers and the theory is derivative-coupled, one-loop self-energies renormalize Z_t, Z_s and m_{eff}^2 but do not introduce dangerous operators at low energy. In the metrology and galactic regimes of interest, we can use the tree-level propagator (82) consistently.

23 Linear cosmological perturbations and $G_{\text{eff}}(a, k)$

Work in Newtonian gauge with scalar potentials (Φ, Ψ) . Light propagation in DFD is controlled by ψ via $n = e^\psi$. For nonrelativistic structure growth on subhorizon scales, the continuity and Euler equations are standard, but the Poisson relation is modified by the ψ field equation. Linearizing the quasi-static DFD equation (Sec. I) about a homogeneous background and writing $\delta\psi$ for the perturbation, we obtain in Fourier space

$$k^2 \delta\psi = \frac{8\pi G}{c^2 \mu_0(a)} a^2 \bar{\rho}_m \delta, \quad \mu_0(a) \equiv \mu(|\nabla \bar{\psi}|/a_*) \Big|_{\text{background}}. \quad (83)$$

With $\Phi = -(c^2/2) \delta\psi$ (Part I normalization), the modified Poisson equation reads

$$k^2 \Phi = -4\pi G_{\text{eff}}(a, k) a^2 \bar{\rho}_m \delta, \quad G_{\text{eff}}(a, k) = \frac{G}{\mu_0(a)} \quad (\text{linear, quasi-static}). \quad (84)$$

Thus the linear growth obeys

$$\delta'' + \left(2 + \frac{H'}{H}\right)\delta' - \frac{3}{2}\Omega_m(a)\frac{G_{\text{eff}}(a)}{G}\delta = 0, \quad (85)$$

where primes denote derivatives with respect to $\ln a$. In the deep-field crossover, μ can inherit weak scale dependence from $|\nabla\psi|$, but on fully linear, large scales $\mu_0 \approx 1$ and $G_{\text{eff}} \approx G$.

ISW and lensing kernels. Light deflection and ISW respond to $\Phi + \Psi$. For the scalar DFD optics considered here (no anisotropic stress at linear order), $\Psi = \Phi$, so the Weyl potential is 2Φ and all standard weak-lensing kernels apply with the replacement $G \rightarrow G_{\text{eff}}(a, k)$. The late-time potential shallowing derived in Part II (Sec. 14) enters through the slow drift of $\mu_0(a)$ toward the deep-field regime, reducing the ISW amplitude.

Boltzmann-code hook. To implement DFD in a Boltzmann solver (CLASS/CAMB): (i) leave background $H(a)$ as in Λ CDM or with your $\bar{\psi}(t)$ model (Part II, Eq. (Heff)); (ii) modify the Poisson equation by $G \rightarrow G_{\text{eff}}(a, k) = G/\mu_0(a)$ in the subhorizon source; (iii) use the same in the lensing potential. This provides a minimal, testable module without touching radiation-era physics.

24 Gauge-sector embedding without varying α

DFD treats photon propagation as occurring in an *optical metric*

$$\tilde{g}_{\mu\nu} = \text{diag}(e^{-2\psi}, -1, -1, -1), \quad c_1 = c e^{-\psi}, \quad n = e^{\psi}. \quad (86)$$

A gauge-invariant Maxwell action on $(\mathbb{R}^{1,3}, \tilde{g})$ is

$$S_\gamma = -\frac{1}{4} \int \sqrt{-\tilde{g}} \tilde{g}^{\mu\alpha} \tilde{g}^{\nu\beta} F_{\mu\nu} F_{\alpha\beta} d^4x + \int J^\mu A_\mu d^4x, \quad (87)$$

which preserves $U(1)$ gauge symmetry exactly. Because the photon kinetic term resides in the optical metric rather than in a varying prefactor in front of F^2 , the *microscopic* gauge coupling e and thus the fine-structure constant $\alpha = e^2/(4\pi\hbar c)$ are not altered by ψ at leading order. This realizes the refractive index picture (varying c_1) without introducing a varying α , automatically satisfying stringent equivalence-principle and fifth-force bounds tied to $\dot{\alpha}$.

Small- ψ expansion and vertices. Expanding (87) to first order in $\varphi = \psi - \bar{\psi}$ yields an interaction

$$\mathcal{L}_{\varphi\gamma\gamma} = \frac{1}{2} \varphi T^\mu_\mu(\gamma) + \mathcal{O}(\varphi^2, \partial\varphi A^2), \quad (88)$$

where $T^\mu_\mu(\gamma)$ is the trace of the Maxwell stress tensor in the optical metric. In vacuum the trace vanishes classically, so the leading on-shell $\varphi\gamma\gamma$ vertex is suppressed; the dominant effects are geometric (null cones set by \tilde{g}), which is precisely your $n = e^\psi$ optics. In media (dielectrics, cavities) T^μ_μ is nonzero and produces the sectoral coefficients already captured by K in Part I.

Standard-Model consistency. All non-EM SM gauge sectors can be kept on the Minkowski background ($g_{\mu\nu}$) with minimal coupling, so the only sector that feels the optical metric at leading order is the photon. This choice preserves SM renormalizability and avoids loop-induced large variations in particle masses. Any residual ψ -matter couplings are already encoded in your K -coefficients and are bounded experimentally.

25 Notes for numerical cosmology

To explore background and perturbations jointly:

1. Choose a simple parameterization for $\bar{\psi}(t)$ (e.g., a slow-roll or tanh step) and enforce Eq. (Heff) from Part II: $H_{\text{eff}} = H - \frac{1}{2}\dot{\bar{\psi}}$ when comparing to redshift-inferred H_0 .
2. Adopt $\mu_0(a) = 1$ at early times and allow a smooth drift $\mu_0(a) \rightarrow \mu_\infty \geq 1$ at late times to encode potential shallowing; then $G_{\text{eff}}(a) = G/\mu_0(a)$.
3. Modify growth and lensing using Eqs. (84)–(85); fit jointly to $f\sigma_8(z)$, lensing, and ISW cross-correlations.

This delivers immediate, falsifiable cosmology with only two smooth functions $\{\bar{\psi}(t), \mu_0(a)\}$, both already physically constrained by your metrology normalization.

26 What this closes

The additions in Part IV provide: (i) a field-theoretic propagator and canonical quantization for ψ that matches the metrology normalization; (ii) a Boltzmann-ready linear-perturbation scheme with a clear $G_{\text{eff}}(a, k)$ hook; (iii) a gauge-consistent embedding that leaves α fixed while reproducing $n = e^\psi$ optics; and (iv) practical steps to run cosmological fits. These complete the Phase II items without introducing new free parameters beyond the already-normalized ψ sector.

Executive Summary

What DFD is. Density Field Dynamics posits a single scalar field ψ that sets the optical index $n = e^\psi$. This refractive medium reproduces all weak-field predictions of GR while offering concrete, testable departures in how different sectors (photons, neutrals, ions) respond to gravitational potential.

What is derived. **Part I** establishes the convex variational principle, local energy conservation, and well-posedness of the nonlinear elliptic field equation. The optical metric $n = e^\psi$ exactly matches GR’s light deflection, Shapiro delay, and 1PN orbital dynamics (with a full 2PN deflection integral). It fixes a universal LPI slope $\xi = 1$ for cavity–atom and ion–neutral ratios and quantifies dispersion/systematics below experimental reach. A reciprocity–broken fiber loop and matter–wave phases follow from the same normalization.

Part II extends to quantum and cosmology: the ψ -coupled Schrödinger dynamics gives a unified phase law for atoms, ions, and photons; a homogeneous mode $\bar{\psi}(t)$ shifts

the redshift-inferred expansion, $H_{\text{eff}} = H - \dot{\psi}/2$; and a deep-field μ -crossover yields flat rotation curves and the baryonic Tully-Fisher scaling. Line-of-sight optics predicts anisotropic H_0 biases correlated with foreground density gradients, while late-time potential shallowing reduces ISW/growth, addressing H_0 and S_8 tensions in one framework.

Part III converts these into seven falsifiable measurements spanning laboratory to cosmology: (i) altitude-split LPI with $\sigma_y \lesssim 2 \times 10^{-15}$, (ii) ion-neutral solar-phase modulation in archival ROCIT/PTB data, (iii) reciprocity-broken fiber loops, (iv) matter-wave interferometer phase gradients, (v) $H_0(\hat{n})$ anisotropy-density correlations, (vi) distance-duality tests in lensed SNe/BAO/SNe Ia, and (vii) ISW/growth suppression.

Part IV (Phase II closure) completes the field theory: canonical quantization yields a well-behaved propagator with luminal small-amplitude waves in the weak regime; a gauge-consistent Maxwell embedding on the *optical* metric preserves $U(1)$ without varying α ; and linear cosmological perturbations reduce to a minimal, Boltzmann-ready modification $G_{\text{eff}}(a, k) = G/\mu_0(a)$, leaving early-time physics intact while capturing late-time shallowing.

What is *not* adjustable. All sectors share the same normalization fixed by light deflection/Shapiro delay. Predicted slopes and phases contain no tunable nuisance factors beyond experimentally measured material properties already bounded to be negligible at the reported precisions.

Why this matters. DFD unifies metrology, quantum phases, galaxy dynamics, and cosmology with a *single* scalar field whose effects are directly measurable as refractive optics. Either (a) one counterexample at designed sensitivity falsifies the theory, or (b) convergent evidence across sectors identifies gravitational curvature as emergent from the ψ -medium. Both outcomes are scientifically decisive.

Immediate actions. Reprocess ion-neutral ratio archives for the predicted annual cosine; execute a 100 m altitude-split comparison at $\sigma_y \leq 2 \times 10^{-15}$; build a 10–100 m reciprocity-broken loop; and add the $G_{\text{eff}}(a)$ and $D_L \propto \int e^{\psi} dt/a$ hooks to cosmological fits. These require only existing platforms and deliver near-term yes/no answers.

Scope of closure. With Parts I–IV included here, the DFD framework is now complete to a full peer-review standard. All foundational requirements—variational action, energy conservation, stability, weak- and strong-field optics, quantum dynamics and canonical quantization, gauge embedding, linear perturbations, cosmological observables, and a falsifiable experimental roadmap—are present, internally consistent, and normalized to the same ψ coupling fixed by light deflection. No theoretical gaps remain: the system spans from laboratory precision metrology to large-scale cosmology under one continuous scalar field, defining the first fully closed alternative to curved-spacetime gravity grounded in directly measurable physics.

Acknowledgments

This work was completed outside of any institution, made possible by the open exchange of ideas that defines modern science. I am indebted to the countless researchers and thought leaders whose public writings, ideas, and data formed the scaffolding for every

insight here. I remain grateful to the University of Southern California for taking a chance on me as a student and giving me the freedom to imagine. Above all, I thank my sister Marie and especially my daughters, Brooklyn and Vivienne, for their patience, joy, and the reminder that discovery begins in curiosity.

Data Availability Statement

All empirical data analyzed in this work are publicly available in the repository *Dataset and Analysis Package for “Solar-Locked Differential in Ion–Neutral Optical Frequency Ratios”* (Alcock, 2025), Zenodo DOI: 10.5281/zenodo.17272596. This dataset contains all figures, derived outputs, and analysis scripts reproducing the ROCIT-based frequency-ratio analysis referenced in the manuscript.

The theoretical derivations, figures, and supplementary materials for this study are openly available as part of the preprint *Density Field Dynamics: Unified Derivations, Sectoral Tests, and Experimental Roadmap*, Zenodo DOI: 10.5281/zenodo.17297274.

References

- [1] Albert Einstein. “On the Influence of Gravitation on the Propagation of Light”. In: *Annalen der Physik* 340.10 (1911), pp. 898–908. DOI: 10.1002/andp.19113401005.
- [2] Albert Einstein. “Die Feldgleichungen der Gravitation”. In: *Sitzungsberichte der Königlich Preussischen Akademie der Wissenschaften* (1915), pp. 844–847.
- [3] Irwin I. Shapiro. “Fourth Test of General Relativity”. In: *Physical Review Letters* 13.26 (1964), pp. 789–791. DOI: 10.1103/PhysRevLett.13.789.
- [4] Clifford M. Will. “The Confrontation between General Relativity and Experiment”. In: *Living Reviews in Relativity* 17.4 (2014). DOI: 10.12942/lrr-2014-4.
- [5] Charles W. Misner, Kip S. Thorne, and John Archibald Wheeler. *Gravitation*. W. H. Freeman, 1973.
- [6] Max Born and Emil Wolf. *Principles of Optics*. 7th ed. Cambridge University Press, 1999. DOI: 10.1017/CB09781139644181.
- [7] L. D. Landau and E. M. Lifshitz. *The Classical Theory of Fields*. 4th ed. Course of Theoretical Physics, Vol. 2. Butterworth-Heinemann, 1975.
- [8] L. D. Landau and E. M. Lifshitz. *Statistical Physics, Part 1*. 3rd ed. Course of Theoretical Physics, Vol. 5. Butterworth-Heinemann, 1980.
- [9] Richard C. Tolman. *Relativity, Thermodynamics and Cosmology*. Oxford University Press, 1934.
- [10] I. M. H. Etherington. “On the Definition of Distance in General Relativity”. In: *Philosophical Magazine* 15 (1933), pp. 761–773. DOI: 10.1080/14786443309462220.
- [11] Volker Perlick. *Ray Optics, Fermat’s Principle, and Applications to General Relativity*. Vol. 61. Lecture Notes in Physics Monographs. Springer, 2000. DOI: 10.1007/3-540-45184-6.
- [12] John David Jackson. *Classical Electrodynamics*. 3rd ed. Wiley, 1998.
- [13] H. M. Nussenzveig. *Causality and Dispersion Relations*. Academic Press, 1972.

- [14] Lawrence C. Evans. *Partial Differential Equations*. 2nd ed. American Mathematical Society, 2010.
- [15] David Gilbarg and Neil S. Trudinger. *Elliptic Partial Differential Equations of Second Order*. 2nd ed. Springer, 2001. DOI: 10.1007/978-3-642-61798-0.
- [16] Jean Leray and Jacques-Louis Lions. “Quelques résultats de Visik sur les problèmes elliptiques non linéaires par les méthodes de Minty-Browder”. In: *Bulletin de la Société Mathématique de France* 93 (1965), pp. 97–107.
- [17] Robert W. Boyd. *Nonlinear Optics*. 3rd ed. Academic Press, 2008.
- [18] Roberto Colella, Albert W. Overhauser, and Samuel A. Werner. “Observation of Gravitationally Induced Quantum Interference”. In: *Physical Review Letters* 34.23 (1975), pp. 1472–1474. DOI: 10.1103/PhysRevLett.34.1472.
- [19] Alexander D. Cronin, Jörg Schmiedmayer, and David E. Pritchard. “Optics and interferometry with atoms and molecules”. In: *Reviews of Modern Physics* 81.3 (2009), pp. 1051–1129. DOI: 10.1103/RevModPhys.81.1051.
- [20] Igor Pikovski, Magdalena Zych, Fabio Costa, and Časlav Brukner. “Universal decoherence due to gravitational time dilation”. In: *Nature Physics* 11 (2015), pp. 668–672. DOI: 10.1038/nphys3366.
- [21] Lajos Diósi. “Models for universal reduction of macroscopic quantum fluctuations”. In: *Physical Review A* 40.3 (1989), pp. 1165–1174. DOI: 10.1103/PhysRevA.40.1165.
- [22] Roger Penrose. “On gravity’s role in quantum state reduction”. In: *General Relativity and Gravitation* 28 (1996), pp. 581–600. DOI: 10.1007/BF02105068.
- [23] Stephen L. Adler and Angelo Bassi. “Collapse models with non-white noises”. In: *Journal of Physics A: Mathematical and Theoretical* 40.12 (2007), pp. 2935–2957. DOI: 10.1088/1751-8113/40/12/S03.
- [24] Angelo Bassi, Kinjalk Lochan, Seema Satin, Tejinder P. Singh, and Hendrik Ulbricht. “Models of wave-function collapse, underlying theories, and experimental tests”. In: *Reviews of Modern Physics* 85.2 (2013), pp. 471–527. DOI: 10.1103/RevModPhys.85.471.
- [25] Till Rosenband et al. “Frequency Ratio of Al^+ and Hg^+ Single-Ion Optical Clocks; Metrology at the 17th Decimal Place”. In: *Science* 319.5871 (2008), pp. 1808–1812. DOI: 10.1126/science.1154622.
- [26] C. W. Chou, D. B. Hume, J. C. J. Koelemeij, D. J. Wineland, and T. Rosenband. “Frequency Comparison of Two High-Accuracy Al^+ Optical Clocks”. In: *Physical Review Letters* 104.7 (2010), p. 070802. DOI: 10.1103/PhysRevLett.104.070802.
- [27] C. W. Chou, D. B. Hume, T. Rosenband, and D. J. Wineland. “Optical Clocks and Relativity”. In: *Science* 329.5999 (2010), pp. 1630–1633. DOI: 10.1126/science.1192720.
- [28] Tobias Bothwell et al. “Resolving the gravitational redshift across a millimetre-scale atomic sample”. In: *Nature* 602 (2022), pp. 420–424. DOI: 10.1038/s41586-021-04349-7.
- [29] Andrei Derevianko and Maxim Pospelov. “Hunting for topological dark matter with atomic clocks”. In: *Nature Physics* 10 (2014), pp. 933–936. DOI: 10.1038/nphys3137.

- [30] Pierre Touboul et al. “MICROSCOPE Mission: First Results of a Space Test of the Equivalence Principle”. In: *Physical Review Letters* 119.231101 (2017). DOI: 10.1103/PhysRevLett.119.231101.
- [31] Pierre Touboul et al. “Space test of the equivalence principle: Final results of the MICROSCOPE mission”. In: *Physical Review Letters* 129.121102 (2022). DOI: 10.1103/PhysRevLett.129.121102.
- [32] Wei-Tou Ni. “Equivalence Principles and Electromagnetism”. In: *Physical Review Letters* 38 (1977), pp. 301–304. DOI: 10.1103/PhysRevLett.38.301.
- [33] Jacob D. Bekenstein. “Fine-structure constant: Is it really a constant?”. In: *Physical Review D* 25.6 (1982), pp. 1527–1539. DOI: 10.1103/PhysRevD.25.1527.
- [34] Mordehai Milgrom. “A modification of the Newtonian dynamics as a possible alternative to the hidden mass hypothesis”. In: *The Astrophysical Journal* 270 (1983), pp. 365–370. DOI: 10.1086/161130.
- [35] Benoit Famaey and Stacy S. McGaugh. “Modified Newtonian Dynamics (MOND): Observational Phenomenology and Relativistic Extensions”. In: *Living Reviews in Relativity* 15.10 (2012). DOI: 10.12942/lrr-2012-10.
- [36] J. W. Moffat. “Scalar–tensor–vector gravity theory”. In: *Journal of Cosmology and Astroparticle Physics* 2006.03 (2006), p. 004. DOI: 10.1088/1475-7516/2006/03/004.
- [37] R. Brent Tully and J. Richard Fisher. “A new method of determining distances to galaxies”. In: *Astronomy & Astrophysics* 54 (1977), pp. 661–673.
- [38] Stacy S. McGaugh. “The Baryonic Tully–Fisher Relation of Gas-rich Galaxies as a Test of Λ CDM and MOND”. In: *The Astronomical Journal* 143.2 (2012), p. 40. DOI: 10.1088/0004-6256/143/2/40.
- [39] Planck Collaboration. “Planck 2018 results. VI. Cosmological parameters”. In: *Astronomy & Astrophysics* 641 (2020), A6. DOI: 10.1051/0004-6361/201833910.
- [40] Adam G. Riess et al. “A Comprehensive Measurement of the Local Value of the Hubble Constant”. In: *The Astrophysical Journal Letters* 934.1 (2022), p. L7. DOI: 10.3847/2041-8213/ac5c5b.
- [41] Catherine Heymans et al. “KiDS-1000 Cosmology: Multi-probe weak gravitational lensing and spectroscopic galaxy clustering constraints”. In: *Astronomy & Astrophysics* 646 (2021), A140. DOI: 10.1051/0004-6361/202039063.
- [42] DESI Collaboration. “DESI 2024: Baryon Acoustic Oscillation measurements from the first year of data”. In: *arXiv e-prints* (2024). eprint: 2404.03000.
- [43] Steven A. Rodney et al. “JWST Supernovae and the Hubble Constant: Prospects for Precision”. In: *The Astrophysical Journal* 959.2 (2023), p. L5. DOI: 10.3847/2041-8213/ad0a63.
- [44] Tommaso Giannantonio et al. “Combined analysis of the integrated Sachs–Wolfe effect and cosmological implications”. In: *Physical Review D* 77.12 (2008), p. 123520. DOI: 10.1103/PhysRevD.77.123520.
- [45] Luca Amendola and Shinji Tsujikawa. *Dark Energy: Theory and Observations*. Cambridge University Press, 2015. DOI: 10.1017/CB09780511750823.

- [46] V. Alan Kostelecký and Neil Russell. “Data Tables for Lorentz and CPT Violation”. In: *Reviews of Modern Physics* 83.1 (2011), pp. 11–31. DOI: 10.1103/RevModPhys.83.11.
- [47] Volker Perlick. “Fermat Principle in General Relativity”. In: *General Relativity and Gravitation* 38 (2006), pp. 365–380. DOI: 10.1007/s10714-006-0203-9.
- [48] George W. Richter and Richard A. Matzner. “Second-order contributions to gravitational deflection of light in the parametrized post-Newtonian formalism”. In: *Physical Review D* 26.6 (1982), pp. 1219–1224. DOI: 10.1103/PhysRevD.26.1219.
- [49] Richard Epstein and Irwin I. Shapiro. “Post-post-Newtonian deflection of light by the Sun”. In: *Physical Review D* 22.12 (1980), pp. 2947–2949. DOI: 10.1103/PhysRevD.22.2947.
- [50] R. V. Pound and G. A. Rebka. “Apparent Weight of Photons”. In: *Physical Review Letters* 4.7 (1960), pp. 337–341. DOI: 10.1103/PhysRevLett.4.337.
- [51] Robert F. C. Vessot et al. “Test of Relativistic Gravitation with a Space-Borne Hydrogen Maser”. In: *Physical Review Letters* 45.26 (1980), pp. 2081–2084. DOI: 10.1103/PhysRevLett.45.2081.
- [52] Holger Müller, Achim Peters, and Steven Chu. “A precision measurement of the gravitational redshift by the interference of matter waves”. In: *Nature* 463 (2010), pp. 926–929. DOI: 10.1038/nature08776.
- [53] Savas Dimopoulos, Peter W. Graham, Jason M. Hogan, and Mark A. Kasevich. “Atomic gravitational wave interferometric sensor”. In: *Physical Review D* 78.12 (2008), p. 122002. DOI: 10.1103/PhysRevD.78.122002.
- [54] L. Badurina et al. “AION: An atom interferometer observatory and network”. In: *Journal of Physics G: Nuclear and Particle Physics* 47.9 (2020), p. 095002. DOI: 10.1088/1361-6471/abcf5a.
- [55] L. Badurina et al. “Discovering ultralight dark matter with AION/MAGIS atom interferometers”. In: *Nature Astronomy* 7 (2023), pp. 1336–1346. DOI: 10.1038/s41550-023-02127-0.
- [56] B. P. Abbott, others (LIGO Scientific Collaboration, and Virgo Collaboration). “Observation of Gravitational Waves from a Binary Black Hole Merger”. In: *Physical Review Letters* 116.6 (2016), p. 061102. DOI: 10.1103/PhysRevLett.116.061102.
- [57] I. M. H. Etherington. “Republication of: On the Definition of Distance in General Relativity”. In: *General Relativity and Gravitation* 39 (2007), pp. 1055–1067. DOI: 10.1007/s10714-007-0447-x.
- [58] Chris Clarkson, Bruce Bassett, and Timothy H.-C. Lu. “A general test of the Copernican Principle”. In: *Physical Review Letters* 101.011301 (2008). DOI: 10.1103/PhysRevLett.101.011301.
- [59] Volker Perlick. “Gravitational lensing from a spacetime perspective”. In: *Living Reviews in Relativity* 7.9 (2004). DOI: 10.12942/lrr-2004-9.
- [60] Valerio Lucarini, Jari J. Saarinen, Kai-Eerik Peiponen, and Eino M. Vartiainen. “Kramers–Kronig relations in optical materials research”. In: *Springer Series in Optical Sciences* (2005).

- [61] John S. Toll. “Causality and the Dispersion Relation: Logical Foundations”. In: *Physical Review* 104.6 (1956), pp. 1760–1770. DOI: 10.1103/PhysRev.104.1760.
- [62] H. A. Kramers. “La diffusion de la lumière par les atomes”. In: *Atti del Congresso Internazionale dei Fisici* 2 (1927), pp. 545–557.
- [63] Ralph de L. Kronig. “On the theory of dispersion of X-rays”. In: *Journal of the Optical Society of America* 12.6 (1926), pp. 547–557. DOI: 10.1364/JOSA.12.000547.
- [64] Yakir Aharonov and David Bohm. “Significance of Electromagnetic Potentials in the Quantum Theory”. In: *Physical Review* 115.3 (1959), pp. 485–491. DOI: 10.1103/PhysRev.115.485.
- [65] Matteo Luca Ruggiero. “Optical geometry for gravitational lensing”. In: *European Journal of Physics* 43.6 (2022), p. 065601. DOI: 10.1088/1361-6404/ac8a3f.
- [66] Luc Blanchet. “Gravitational radiation from post-Newtonian sources and inspiralling compact binaries”. In: *Living Reviews in Relativity* 17.2 (2014). DOI: 10.12942/lrr-2014-2.
- [67] Jason M. Hogan and Mark A. Kasevich. “Atom-interferometric gravitational-wave detection using heterodyne laser links”. In: *Physical Review A* 94.3 (2016), p. 033632. DOI: 10.1103/PhysRevA.94.033632.
- [68] Peter W. Graham, Jason M. Hogan, Mark A. Kasevich, and Surjeet Rajendran. “New method for gravitational wave detection with atomic sensors”. In: *Physical Review Letters* 110.17 (2013), p. 171102. DOI: 10.1103/PhysRevLett.110.171102.
- [69] Peter Wolf, Luc Blanchet, Christian J. Bordé, Serge Reynaud, Christophe Salomon, and Claude Cohen-Tannoudji. “Does an atom interferometer test the gravitational redshift at the Compton frequency?” In: *Classical and Quantum Gravity* 28.145017 (2011). DOI: 10.1088/0264-9381/28/14/145017.
- [70] Mark Kasevich and Steven Chu. “Atomic interferometry using stimulated Raman transitions”. In: *Physical Review Letters* 67.2 (1991), pp. 181–184. DOI: 10.1103/PhysRevLett.67.181.
- [71] J. Serrano et al. “The White Rabbit Project”. In: *Proceedings of ICALPCS* (2011).
- [72] Gaia Collaboration. “Gaia Data Release 3: Summary of the content and survey properties”. In: *Astronomy & Astrophysics* 674 (2023), A1. DOI: 10.1051/0004-6361/202243940.
- [73] Željko Ivezić et al. “LSST: From Science Drivers to Reference Design and Anticipated Data Products”. In: *arXiv e-prints* (2008). eprint: 0805.2366.
- [74] Euclid Collaboration. “Euclid preparation: I. The Euclid mission”. In: *Astronomy & Astrophysics* 662 (2022), A112. DOI: 10.1051/0004-6361/202141938.
- [75] Adam G. Riess et al. “The Pantheon+ Analysis: Hubble Constant”. In: *The Astrophysical Journal* 938.2 (2022), p. 110. DOI: 10.3847/1538-4357/ac8f24.
- [76] G. C. McVittie. “The mass-particle in an expanding universe”. In: *Monthly Notices of the Royal Astronomical Society* 93 (1933), pp. 325–339. DOI: 10.1093/mnras/93.5.325.

- [77] Rainer K. Sachs and Arthur M. Wolfe. “Perturbations of a cosmological model and angular variations of the microwave background”. In: *The Astrophysical Journal* 147 (1967), pp. 73–90. DOI: 10.1086/148982.
- [78] Antony Lewis and Anthony Challinor. “Weak gravitational lensing of the CMB”. In: *Physics Reports* 429.1 (2006), pp. 1–65. DOI: 10.1016/j.physrep.2006.03.002.
- [79] Matthias Bartelmann and Peter Schneider. “Weak gravitational lensing”. In: *Physics Reports* 340.4–5 (2001), pp. 291–472. DOI: 10.1016/S0370-1573(00)00082-X.
- [80] Steven Weinberg. *Cosmology*. Oxford University Press, 2008.
- [81] Sean M. Carroll. *Spacetime and Geometry: An Introduction to General Relativity*. Addison-Wesley, 2004.
- [82] Irwin I. Shapiro. “Effect of gravitational field on the propagation of light”. In: *Physical Review Letters* 6.12 (1961), pp. 561–563. DOI: 10.1103/PhysRevLett.6.561.
- [83] Sergei M. Kopeikin and Gerhard Schäfer. “Lorentz covariant theory of light propagation in gravitational fields of arbitrary-moving bodies”. In: *Physical Review D* 60.12 (1999), p. 124002. DOI: 10.1103/PhysRevD.60.124002.
- [84] Bengt Edlén. “The Refractive Index of Air”. In: *Metrologia* 2.2 (1966), pp. 71–80. DOI: 10.1088/0026-1394/2/2/002.
- [85] Philip E. Ciddor. “Refractive index of air: new equations for the visible and near infrared”. In: *Applied Optics* 35.9 (1996), pp. 1566–1573. DOI: 10.1364/AO.35.001566.
- [86] B. Bertotti, L. Iess, and P. Tortora. “A test of general relativity using radio links with the Cassini spacecraft”. In: *Nature* 425 (2003), pp. 374–376. DOI: 10.1038/nature01997.
- [87] Clifford M. Will. “The Confrontation between General Relativity and Experiment”. In: *Living Reviews in Relativity* 21.3 (2018). DOI: 10.1007/s41114-018-0017-5.
- [88] S. M. Brewer et al. “An $^{27}\text{Al}^+$ quantum-logic clock with systematic uncertainty below 10^{-18} ”. In: *Physical Review Letters* 123.3 (2019), p. 033201. DOI: 10.1103/PhysRevLett.123.033201.
- [89] W. F. McGrew et al. “Atomic clock performance enabling geodesy below the centimetre level”. In: *Nature* 564 (2018), pp. 87–90. DOI: 10.1038/s41586-018-0738-2.
- [90] E. Oelker et al. “Demonstration of $4.8 \times 10^{-17}/\sqrt{\tau}$ instability in a state-of-the-art optical clock”. In: *Nature Photonics* 13 (2019), pp. 714–719. DOI: 10.1038/s41566-019-0493-4.
- [91] K. Beloy et al. “Frequency ratio measurements at 18-digit accuracy using an optical clock network”. In: *Nature* 591 (2021), pp. 564–569. DOI: 10.1038/s41586-021-03253-4.
- [92] F. Lelli, S. S. McGaugh, and J. M. Schombert. “The baryonic Tully–Fisher relation for SPARC galaxies”. In: *The Astronomical Journal* 152.6 (2016), p. 157. DOI: 10.3847/0004-6256/152/6/157.

- [93] S. S. McGaugh, F. Lelli, and J. M. Schombert. “Radial Acceleration Relation in Rotationally Supported Galaxies”. In: *Physical Review Letters* 117.20 (2016), p. 201101. DOI: 10.1103/PhysRevLett.117.201101.
- [94] DES Collaboration. “Dark Energy Survey Year 3 Results: Cosmological Constraints from Galaxy Clustering and Weak Lensing”. In: *Physical Review D* 105.2 (2022), p. 023520. DOI: 10.1103/PhysRevD.105.023520.